# Utilizing the L-PSJA for controlling cylindrical wake flow

I.H. Ibrahim[1], M. Skote*[1]

[1]School of Mechanical & Aerospace Engineering, Nanyang Technological University, 50

Nanyang Avenue, Singapore 639798

Tel: +6567904271/ FAX: +6567924062

*Corresponding author. Email: mskote@ntu.edu.sg

**Abstract**

This study concerns the utilization of the Linear Plasma Synthetic Jet Actuator (L-PSJA) as a flow control device to suppress von Kármán vortex streets (VKS) formation in a cylindrical wake flow. The investigation is characterised by a low Reynolds number of 100, producing steady and laminar vortices downstream of the cylinder. Two parameters were varied in the analysis: The voltage setting of the downstream exposed electrode (ϕmax2) and angular position of the L-PSJA (n). A modified form of the Suzen-Huang model, previously shown to yield reliable results, is used to simulate the induced jets of the L-PSJA. The results demonstrate that of the twelve permuted configurations that were investigated (four for n and three for ϕmax2), five combinations were able to suppress the formation of the VKS. The suppression is characterized by uniform velocity profiles downstream of the cylinder.

## 1. Introduction

Flow around a circular cylinder is one of the fundamental problems in aerodynamics that have been investigated thoroughly by several researchers. The cylindrical wake flow is an important part of many engineering applications, including wake turbulence, acoustic noise, and lift/drag forces on bodies. A comprehensive review of cylinder flow is given in (Williamson, 1996) and (Zdravkovich, 1997). Also the work of Kozlov (2010) provides an account of the flow around a circular cylinder in the context of plasma actuator control. Here, we provide a summary of the three sources.

A variety of flow regimes exists due to the presence of the cylinder. The behaviour of the boundary layer, shear layer, as well as the vortex structure within each regime are strongly dependent on the Reynolds number of the flow. At very low Reynolds numbers (below Re = 4), the flow is fully laminar and firmly attached to the cylinder geometry. As Reynolds number increases to 5, the flow separates, and steady separation bubbles are formed. At Reynolds number of 45 to about 100, an array of laminar vortices is formed. In this state, the flow pattern is described as a von Kármán vortex street (VKS). The transition to turbulent flow gradually moves upstream from the far wake to the near wake for $180 < Re < 400$. The main features of the flow pattern in the vortex street remain essentially the same until the Reynolds number reach $4x10^5$, except that the transition occurs at various downstream positions.

There are several main approaches in the study of flow control of flow around circular cylinders because the objectives of the flow control are multi-faceted. Control of separation, which suppresses the VKS, is one example. The advantages of controlling the vortex shedding include reducing drag, increasing lift, suppressing noise, decreasing vibration, and increasing mixing or heat transfer. To control the vortex shedding, researchers have considered both active and passive control, and with or without feedback control. Previous studies into the flow control around a circular cylinder can be categorized into two forms, namely geometric or flow field modifications. In geometrical modifications, cylindrical wake studies have been performed with an inclusion of splitter plates, as well as a smaller secondary cylinder placed in the wake region. The main cylinder could also be oscillated transversely, or rotated, in order to suppress vortex shedding. Flow field modifications include the placing of bleeding, blowing or suction apparatus in the vicinity of the wake field to reduce shedding. These modifications are also most often accompanied by a control feedback loop.

For the purpose of the present investigation, an open loop approach is taken, while the active flow control is realized by utilizing plasma actuators which have evolved in the last two decades. Reviews concerning the plasma actuator can be found in (Corke et al., 2010) and (Moreau, 2007). Plasma actuators have been tested in various applications, including separation control on a delta wing (Zhang et al., 2010), turbine blades (Huang et al., 2006, Rizzetta and Visbal, 2007) and airfoils (Post and Corke, 2006, Huang et al., 2007, Benard et al., 2009). The wide range of applications in the aerospace industry highlights the potential of the plasma actuator as a separation control device.

The advantages of using plasma actuators for controlling airflow are that these actuators have no moving parts and are light. The plasma actuator also results in real-time changes to the aerodynamic system because the fundamental working mechanism of plasma stems from the motion of charge particles that are governed by a varying electric field.

Experimental investigations of cylinder wake vortex control using plasma actuators are plentiful; see e.g. the work by Jukes and Choi (2009) and references therein. Previous investigations by Thomas *et al.* (2008) utilized surface mounted plasma actuators on a circular cylinder in cross flow. The results showed that steady operation of the actuators were able to drastically reduce the degree of flow separation, and eliminate the associated VKS. Artana *et al.* (2003) utilized a wire-to-plate plasma actuator geometry to control vortex shedding. The wire was placed at the stagnation point of the flow, while the plate was flushed at $180^{\circ}$ angle relative to the flow. Vortex shedding control by two circular cylinders using plasma actuators was conducted by Asghar and Jumper (2009).

All of the above mentioned studies were focused on turbulent flows using experimental methodology to investigate the applicability of plasma actuators for flow control. A recent study (Igarashi et al., 2014 ) utilized Direct Numerical Simulation (DNS) to investigate flow control around a cylinder by plasma actuators. The results indicated that the two-dimensional forcing is effective in drag reduction.

In the present numerical investigation, we utilize the Linear Plasma Synthetic Jet Actuator (L-PSJA) to control vortex shedding in cylindrical cross flow. The term L-PSJA was initially coined by Santhanakrishnan et al. (2009), in which he describes the application essentially as a ‘geometric variation’ to the initial plasma actuator that can be used to produce ‘zero-mass flux’ similar to that created by mechanical devices. To the author’s knowledge, the present work is the first study illustrating the capability of L-PSJA to suppress vortex shedding. Here, the goal is to find the optimum configuration of the L-PSJA that minimizes lift and drag oscillations caused by the VKS. The Reynolds number, based on the diameter of the cylinder, is constant at 100. At this instance, regular Kármán vortex shedding occurs and the resulting flow profiles are completely laminar. Since the flow is laminar, the Navier-Stokes equations can be solved directly (without turbulence modelling) although the requirement on resolution is much less restricted compared to direct numerical simulations of turbulent flows (see further references in e.g. Skote, 2014). The geometry of the cylinder wake flow model is based on a benchmark computation study in (Schafer and Turek, 1996).

The physical geometry of the problem is presented in section 2, while the numerical plasma model is described in section 3. Details of the software will be mentioned in section 4, together with grid independence tests. Results will be presented in section 5. We compare lift and drag coefficient plots for the cylinder without the L-PSJAs, as well as with various L-PSJA configurations in sections 5.1 and 5.2 respectively. In addition, we include velocity surface plots of the wake flow for the different L-PSJA configurations in section 5.4. We end with discussions and conclusions in section 6.

## 2. Problem geometry and plasma actuator configuration

Figure 1 represents the modelling domain in our simulation. The cylinder is placed in a channel of length 2.2m and height 0.4m. The diameter of the cylinder is 0.2 m. The inlet boundary condition is at the left side of the domain and is set with a mean velocity of 1 m/s. The cylinder is offset (0.01 m) from the centre in order to introduce asymmetries in the flow, with the possibility to grow due to instabilities, which is crucial for the creation of the VKS. The outlet boundary condition is set at the right hand side of the domain. No-slip boundary conditions are set at the top and bottom sides of the domain, as well as the circumference of the cylinder. Two L-PSJAs are placed at the top and bottom parts of the cylinder, as indicated by the lines within the cylinder.

A zoomed-image of the cylinder together with the L-PSJAs is shown in Figure 2. The L-PSJAs are placed at various angles relative to surface of the cylinder as indicated in Figure 2, where *n* represents the angle between the mean flow (at stagnation point) and leading exposed electrode. The voltage of the downstream exposed electrode ($\phi_{max2}$) was also altered to enable the L-PSJAs to vector the induced jets. The voltage settings of the exposed electrodes are increased to 20 kV in this viscosity dominated flow, to ensure sufficient induce velocity is produced to affect the VKS in the wake field.

Finally, the details of the L-PSJA itself is illustrated in Figure 3. In this study we utilize the plasma actuator, more specifically the Single Dielectric Barrier Discharge (SDBD), as a synthetic jet with zero net mass flux. This is accomplished by using two exposed and one encapsulated electrode, as shown in Figure 3, to form the L-PSJA. This is a modification to the design of the SDBD plasma actuator by a second exposed electrode placed downstream from the first. The position of the electrodes produces a net upward directional body force, inducing flow in a similar upward direction. The design resembles a synthetic jet discharging from a rectangular opening, which can be considered to be nominally two dimensional. The interaction between the synthetic jet and a cross flow over a solid surface can lead to local displacement of the cross flow, inducing a modification of flow boundary and alter local pressure and vorticity distributions. In addition to the amplitude of the induced jet, also the angle of the jet can be manipulated by applying different voltages on the downstream and upstream exposed electrodes. A detailed description of the basic flow field as well as vectoring ability can be found in (Ibrahim and Skote, 2012).

## 3. Model description and computational methodology

The Suzen and Huang (S-H) model was chosen against other physics-based models due to its ability to simulate the electric field and charge density variables separately. These two variables constitute the Lorentz body force that is inserted into the Navier-Stokes equation. The fluid and S-H model are described extensively (Ibrahim and Skote, 2010, Ibrahim and Skote, 2013, Ibrahim and Skote, 2011, Ibrahim and Skote, 2014). In the present investigation we utilized a modified form of the S-H model, which was shown to yield results comparable with experimental investigations of the L-PSJA in the recent study by Ibrahim and Skote (2012). Below is a summary of the modified model provided.

### *3.1 Plasma model*

The plasma actuator model designed by (Suzen et al., 2005) studied the implication of splitting the total electric potential term ($\Phi$) into two parts: one being influenced by external electric field ($\phi$), and the other potential affected by the net charge density ($\varphi$). This technique had been applied to flow control in turbine blades (Suzen et al., 2005, Suzen and Huang, 2006, Suzen et al., 2007, Reasor Jr et al., 2007) to achieve reduction in flow separation. The equations governing the plasma actuator are:

$$\nabla.(\varepsilon_r \nabla \phi^*) = 0 \tag{1}$$

and

$$\nabla.(\varepsilon_r \nabla \rho_c^*) = \rho_c^* / \lambda_D^2 \tag{2}$$

where $\varepsilon_r$ is the relative permittivity, $\lambda_D$ is the Debye length, $\phi^*$ and $\rho_c^*$ are the non-dimensionalised electric field potential and surface charge density, respectively. The physical dimensional quantities $\phi$ and $\rho_c$ can be retained from

$$\phi = \phi^* \phi_0(\tau) \tag{3}$$

$$\rho_c = \rho_c^* \rho_{c,0}(\tau) \tag{4}$$

where

$$\phi_0(\tau) = \phi_{max} \times f(\tau) \tag{5}$$

$$\rho_{c,0}(\tau) = \rho_{c,max} \times f(\tau) \tag{6}$$

$\phi_{max}$ (V) and $\rho_{c,max}$ (C/m$^3$) refer to the maximum amplitude and the maximum charge density of the AC voltage supplied. The function $f(\tau)$ for the AC voltage source appearing in equations (5) and (6) is:

$$f(\tau) = \sin(\frac{\pi}{2}\tau) \tag{7}$$

where $\tau$ refers to a non-dimensionalised time quantity which is related to the frequency $\omega$ as:

$$\tau = \omega t \tag{8}$$

where $\omega$ (Hz) refers to the frequency of the AC voltage supply and is equal to 4.5 kHz.
Thus, the model consists of solving equations (1) and (2) with suitable boundary conditions. Finally, the Lorentz body force which is used in the Navier-Stokes equations is obtained through:

$$F_b = \rho_c(-\nabla \phi) \tag{9}$$

The two equations governing the non-dimensionalised electric field potential and the surface charge potential can be solved initially before the Navier-Stokes equation as these equations do not contain a time derivative term.
The boundary condition for the upper electrode for $\phi^*$ is set to unity so that once $\phi^*$ is determined, the dimensional value $\phi$ can be obtained at any given time by multiplying the distribution with the corresponding value $\phi_o(\tau)$ given by (5). Similarly, the boundary

condition for the lower electrode for $\rho_c^*$ is set to unity. This allows the dimensional value $\rho_c$ to be obtained by multiplying the non-dimensionalised distribution $\rho_c^*$ with the corresponding value $\rho_{c,o}(t)$ given in (6).
Finally, equations (1), (2) and their boundary equations are shown together with the geometries in Figure 4 and Figure 5, respectively. The terms GE and BC refer to governing equation and boundary conditions respectively. The BCs are described next.

### *3.2 Boundary conditions*

In our modified S-H model, two new BCs are introduced for the Kapton surface above the encapsulated electrode. These two new BCs are the main components of the modified S-H model used in the simulations. They are denoted BC3 (for equation (1), shown in Figure 4), and BC7 (for equation (2), shown in Figure 5) and are described below. Both potentials are scaled using a $\phi_{max_}$value. However, $\phi_{max,1}$ is maintained constant at 20 kV, while $\phi_{max,2}$ is varied at 0 kV, 10 kV and 20 kV. This is consistent with the basis for the S-H model which consists of 1) non-dimensional solution of the forcing function, and 2) rescaling the solution to a desired voltage setting ($\phi_{max}$). Thus, every combination of $\phi_{max1}$ and $\phi_{max2}$ is calculated separately. A more detailed description can be found in (Ibrahim and Skote, 2011, Ibrahim and Skote, 2012).

#### *3.2.1 Dielectric shielding*

The 'dielectric shielding' condition for the non-dimensionalised electric potential shown as BC3 in Figure 4 describes a thin layer of thickness $\lambda_D$ and relative bulk permittivity $\varepsilon_{\mathrm{r,m}}$. The terms $\nabla_n$ and $\nabla_t$ describe the normal and tangential derivatives of the non-dimensionalised electric potential variable. The boundary condition equates the normal and tangential derivatives of the dimensionless electric potential, to produce a thin layer across the boundary that shields the electric field formed by the two electrodes. This results in a spread of the electric potential and electric field magnitude across the boundary.

#### *3.2.2 Dissipation and propagation characteristics*

For the equation governing the non-dimensionalised charge density, the original boundary condition used in the S-H model resulted in an instantaneous charge density growth along the boundary of the lower electrode that propagates in the normal direction (upwards) of the dielectric surface. This propagation direction is different compared to the results obtained by charge transport models, where propagation towards the right-side of the exposed electrode was obtained (Boeuf and Pitchford, 2005, Mamunuru et al., 2009). This motion of the surface charge corresponds to the physics of the plasma actuator, in which streamers originate from the exposed electrode and travels along the dielectric surface. These streamers dissipate and propagate from the exposed electrode and have not been shown in previous S-H models.

We imposed the boundary modifications as described in (Ibrahim and Skote, 2011) at the interface above the encapsulated electrode as shown in Figure 5. To replicate dissipation and propagation characteristics, two boundary conditions are combined. They form a new boundary condition which is obtained by multiplying BC9 with BC10 or BC11. These boundary conditions are written as:

BC9: $\exp\left(-\frac{\left(\frac{x-x_1}{x_3}\right)^2}{2\sigma^2}\right)$

(10)

BC10: $\exp(-(x-x_1)-\tau) \quad x > x_1$

(11)

BC11: $\exp(-(x-x_2)-\tau) \quad x < x_2$

(12)

where $x_1$ and $x_2$ are the x-coordinates of the left and right edges of the encapsulated electrode. The terms $x_3$ and $\sigma$ are determined by the width of the normal distribution function and are taken as 2 x $10^{-3}$ m and 0.3 respectively as used previously by (Ibrahim and Skote, 2011, Ibrahim and Skote, 2012).

### *3.3 Simulation procedure*

The values for $\lambda_D$ and $\rho_{c,max}$ are chosen as 2 x $10^{-4}$ m and 3 x $10^{-4}$ C/m$^3$ respectively. $\phi_{max}$ is set independently on the upstream ($\phi_{max1}$) and the downstream ($\phi_{max2}$) electrode, with $\phi_{max1}$ = 20 kV and $\phi_{max2}$ varied between 0 and 20 kV. The equations governing the L-PSJAs are solved until $\tau$ = 1.0, similar to the previous study done on the SDBD (Ibrahim and Skote, 2011) as well as the single L-PSJA (Ibrahim and Skote, 2012). At $\tau$ = 1, the peak voltage of first half cycle is reached. The results at this instant are assumed as the pseudo-steady state of the actuator.

The pseudo-steady state assumption is based on the three factors. Firstly, the plasma discharge has a characteristic time that is several orders lower than the electric field. The AC period required to power the actuator is long ($10^{-4}$s) compared to the time needed for the charges in the plasma to redistribute ($10^{-8}$s - $10^{-9}$s). Similar physics-based modelling assumptions have been made in (Orlov et al., 2007, Orlov et al., 2006). Secondly, the fluid flow response to the induced body force is much slower than the AC period, and hence the time scale of the fluid is much larger ($10^{-2}$s) than that of the applied plasma dynamics. Thirdly, the sinusoidal discharge is predominantly characterized in the first half-cycle, when the exposed electrodes are acting as cathodes. This has been verified by the results obtained in various experiments (Forte et al., 2007, Porter et al., 2007). In the present study we will therefore focus on one time instant (at the peak of the first AC cycle) in the same way as was done in the investigations by (Jayaraman et al., 2007, Jayaraman et al., 2006).

Since the electric potential (1) and surface charge (2) equations are decoupled from the Navier-Stokes (N-S) equations, a segregated solving approach can be used. The modified form of the S-H model is initially solved until $\tau$ = 1.0. The solutions are then inserted to the fluid model, which solves the N-S equation until t = 10s. A parametric solver was also used to investigate two scalar parameters, which are the voltage setting of the downstream exposed electrode ($\phi_{max2}$) and angular position of the L-PSJA (*n*). The values chosen for $\phi_{max2}$ were 0 kV, 10 kV and 20 kV. The values were chosen to ensure that the induced jets would sufficiently alter the characteristics of the incoming flow. For *n*, the values used in the investigation were 0°, 40°, 80° and 120°, to ensure that the total circumference of the cylinder is investigated.

The above described simulation technique was used by Ibrahim and Skote (2012) for simulating a single L-PSJA, and good agreement with the experimental investigation (Santhanakrishnan et al., 2009) of the same case was obtained. Thus, although no experimental data is available for the present configuration, we are confident that the results can be realized in an experimental setting.

## 4. Computational method and grid independence

Since the problem is both electrostatics and fluid dynamic in nature, we have used a finite element computational package capable of handling the multiphysics features (COMSOL, 2012). The method used to solve the time-dependent problem was the backward differentiation formula (BDF) which is described in (Hindmarsh et al., 2005).

We have previously performed a verification analysis which showed that the choice of grid settings in the order of $10^{-4}$ m was adequate for producing numerically acceptable results. Similar grid settings were also used for the L-PSJA geometry (Ibrahim and Skote, 2012), indicating negligible change in results when compared to a finer grid.

To verify the grid independence for the present geometry, a simulation with a grid consisting of twice the amount of elements was performed. The coarse grid was defined such that the regions near the electrodes had a maximum grid size of $10^{-4}$ m. The fine grid setting had a maximum size of $5x10^{-5}$ m. The two settings are shown in Figure 6 and Figure 7, in which the simulation domain and a close up of the top L-PSJA is shown.

In Figure 8 we compare the time histories of lift and drag coefficient of the cylinder in the simulation (with no plasma activated). The maximum lift and drag coefficient obtained by our simulation were 0.42 and 1.57 respectively, which is similar to the values obtained by Mittal and Raguvanshi (2001). Oscillations of the lift coefficient occur when t = 5s. The amplitude of the oscillations increases and remains symmetrical at t = 7.5s. For the drag coefficient, both mesh settings record an almost instantaneous increase to about 3. As the lift and drag coefficients indicate that the chosen discretization size exhibit negligible variations, the coarse grid setting mentioned above was used for the studies presented in the next section.

## 5. Results

Lift and drag coefficient plots are compared for instances when the plasma actuator is turned on and off, in section 5.1 and 5.2 respectively, while section 5.3 is devoted to the drag force balance. In section 5.4, we compare the velocity surface plots of the simulation domains.

### *5.1 Lift Coefficient*

The lift coefficient values for the different configurations are shown in Figure 9. The solid, dotted and dashed lines represent the lift coefficient when $\phi_{max2}$ are 0 kV, 10 kV and 20 kV respectively ($\phi_{max1}$ is kept constant at 20 kV). The solid line with asterisk line represents the results for the simulation when plasma actuators are not used. Note that the lift force calculated is the total lift, including the direct forcing on the cylinder from the actuator. While this effect influences the magnitude of the lift force, the direct force imparted by the actuator is steady and will not affect the oscillations other than indirectly by altering the flow field around the cylinder. The direct forcing from the actuator is further discussed in Section 5.3.

With the placement of actuators, there is an initial dip in the lift coefficient, from 0 to 0.5s. This is due to the activation of the L-PSJAs. After 0.5 s, there may be oscillations, depending on the success of the L-PSJAs to suppress the VKS. The oscillations also exhibit x-axis asymmetry. For example, when $n$ is $0^{\circ}$, the maximum and minimum amplitudes of the lift coefficient were 0.25 and -0.55 respectively. When $n$ is $120^{\circ}$, the maximum and minimum amplitudes of the lift coefficient were 1.2 and -1.6 respectively. For comparison, when the actuators are turned off, the VKS is perfectly symmetrical and oscillates between 0.4 and -

0.4. This suggests that the addition of the L-PSJAs accentuates the offset of the cylinder from the centre of the inlet flow.

When $n$ is $0^{\circ}$, the presence of the L-PSJAs with the three $\phi_{max2}$ values does not help to reduce lift coefficient oscillations. On the contrary, the actuators results in an earlier onset of oscillations which can be seen initiating from 0 to 4 s, after which the oscillations remain asymmetric as mentioned earlier. When $n$ is $40^{\circ}$ and $\phi_{max2}$ is 0 kV, the lift coefficient plot begins with a dip and then reaches a plateau for the remaining part of the simulation. This shows that the L-PSJAs are able to suppress the formation of VKS, resulting in zero lift coefficient oscillations. Similar features (dip and plateau) are also seen when $n$ is $80^{\circ}$ and $120^{\circ}$ for $\phi_{max2}$ values of 0 kV and 10 kV. For these cases, the main flow at the separation region is reenergised by the induced L-PSJAs jets, which follow the convex contours of the cylinder. When $\phi_{max2}$ is 20 kV, at all $n$ values, the L-PSJAs jets promote the formation of oscillations.

Thus, for the symmetric cases, either when $n$ is zero or the voltage difference is zero, VKS is promoted. When the L-PSJAs are placed at $40^{\circ}$, only the case with largest voltage difference ($\phi_{max2}$=0 kV) can suppress the VKS. On the other hand, when $n$=$80^{\circ}$ or $120^{\circ}$, two cases ($\phi_{max2}$=0 kV and 10 kV) can subdue the VKS. Hence, the vectoring of the artificial zero-net mass flux jets is crucial for the successful annihilation of the VKS.

The RMS and mean values of the oscillatory regions are shown in Figure 10. Here, only the data from seven seconds and onward is used for the analysis. Some qualitative results that can be observed from Figure 9 can be quantified in Figure 10, e.g. the strong oscillations observed (Figure 9) for $n$=$120^{\circ}$, $\phi_{max2}$=20 kV result in the largest observed RMS value (Figure 10).

Figure 11 shows the Strouhal frequencies of the cases with vortex shedding. Again, the data is taken from the asymptotic state after 7 s. The results indicate that the dominant frequencies are in the range of 2.5 – 3 Hz.

### *5.2 Drag Coefficient*

The drag coefficient values for the different configurations are shown in Figure 12. Similar to the lift coefficient plots, the solid, dotted and dashed lines represents graph for lift coefficient when $\phi_{max2}$ are 0 kV, 10 kV and 20 kV respectively.

Contrary to the initial dip seen in the lift coefficient plots, the drag coefficient plots show an increase from 0 s to 0.5 s. This is due to the activation of the L-PSJAs jets, before the main flow impinges on the cylinder. The drag coefficient then plateaus either to a straight line, or forms minor fluctuations that persists throughout the simulation. These minor fluctuations coincide with the oscillations seen in the lift coefficient plots, and are due to the formation of the VKS. The fluctuations increase in magnitude when $\phi_{max2}$ is 20 kV and $n$ is $80^{\circ}$ and $120^{\circ}$, from 3.5 s onwards. This augmented amplitude was similarly observed for the lift coefficient (Figure 9). Hence, a non-fluctuating drag coefficient corresponds to the suppression of the VKS. However, no fluctuations for the case of $n$=$40^{\circ}$ and $\phi_{max2}$ =10 kV can be detected in Figure 12. The lift coefficient for this case (Figure 9), on the other hand, shows that the VKS does exist, albeit the amplitude is suppressed. Furthermore, we can observe from Figure 12 that, generally, the cylinder experiences a larger drag coefficient when $n$ is increased. When $n$ is $0^{\circ}$ and $\phi_{max2}$ is 20 kV, a drag coefficient reading of -1.5 is recorded. The negative drag coefficient implies that the drag force exerted by the L-PSJA has a larger value compared to the drag force produced by the mean flow. For the same angle (n=$0^{\circ}$), the case with $\phi_{max2}$ =10 kV exhibits nearly zero drag, which means that the forces balances each other, while for $\phi_{max2}$ =0 kV, the drag coefficient is closer to the original value. When $n$ is $40^{\circ}$, the $\phi_{max2}$ =0 kV case yields a drag coefficient larger than the original one, while it remains lower for the other two cases. For n=$80^{\circ}$ and $120^{\circ}$, all cases result in larger drag. When $n$ is $120^{\circ}$ and

$\phi_{max2}$ is 20 kV, the drag coefficient is about 3.7, which is the maximum value observed in the present investigation.

The RMS and mean values of the oscillatory regions are shown in Figure 13. In this case, obviously, the two quantities remain nearly identical since the signal exhibits only minor fluctuation around a mean value. However, an interesting trend is observed in that the drag increases with the angular position for all $\phi_{max2}$ (in agreement with the conclusions drawn from Figure 12 above), although the steepest gradient is detected for $\phi_{max2}$ =20 kV.

The corresponding dominant frequencies for drag are from 5.5-6 Hz as shown in Figure 14. Due to the alternating vortex wake, the oscillations in lift force occur at the vortex shedding frequency while the oscillations in drag force occur at twice the vortex shedding frequency.

Thus, for all cases which were proven to suppress the VKS, the drag has increased (compared to the uncontrolled case). The velocity surface plots shown in section 5.4 will further illustrate the characteristics seen in the lift and drag coefficient plots. Before that, however, we will investigate in further detail the negative drag coefficient observed when *n* is $0^{\circ}$ and $\phi_{max2}$ is 20 kV.

### *5.3 Cylindrical Drag Force Balance*

Since the actuator is influencing the flow with a volume force, then the same force will act on the cylinder through the actuator in the opposite direction. This volume force is included when calculating the lift and drag coefficients. In order to separate the contributions from the direct forcing of actuator and the effect of the changes in aerodynamic force by influencing the flow field, the cylindrical drag force balance is considered through the equation VF+AF=ML, where VF is the magnitude of the volume force (imparted by the actuators), AF is the magnitude of aerodynamic force (experience by the cylinder), and ML is the total drag, or the magnitude of momentum loss (integration at the outlet of the simulation domain).

For the uncontrolled case (with no actuator), there is no volume force, therefore the aerodynamic drag forces experienced by the cylinder is equal to the momentum loss in the cylinder wake. This is shown in Figure 15. Note that the units are in N/m2.

For a controlled case the volume force will contribute to the total drag. For the cases with $n=0^{\circ}$, the volume force will be negative, and particularly for the case of $\phi_{max2}$ =10 kV this force is exactly equal to the aerodynamic force, hence leading to zero drag coefficient as illustrated in Figure 12. For the case when *n* is $0^{\circ}$ and $\phi_{max2}$ is 20 kV, a negative total drag is obtained which is manifested as a negative drag coefficient (see Figure 12). The graphical representation of the force balance is shown in Figure 16.

The negative total drag (the momentum loss in Figure 16) experienced by the cylinder when *n* is $0^{\circ}$ and $\phi_{max2}$ is 20 kV is due to the larger volume force acting on the cylinder and in the opposite direction to the aerodynamic force.

A tabular representation of the volumetric and aerodynamic force contributions (in percentages) for the different cases is shown in Table 1. It demonstrates that only for Case 3 (which is illustrated in Figure 16), the volume force is larger than the aerodynamic drag and acting in the opposite direction. The largest volume force contribution occurs for Case 7, when n = 80º and $\phi_{max2}$ = 0 kV.

### *5.4 Velocity surface plots*

The velocity plots for the different configurations at t = 10 s are shown in Figure 17. The plots confirm the observations made for the lift coefficients in Figure 9. In the twelve configurations that were investigated (three for $\phi_{max2}$ and four for *n*), five configurations were able to suppress the formation of the VKS. This is characterized by the uniformed velocity downstream of the cylinder. The configurations were: $n = 40^{\circ}$ $\phi_{max2} = 10$ kV, $n = 80^{\circ}$ $\phi_{max2} = 0$ kV and 10 kV, $n = 120^{\circ}$ $\phi_{max2} = 0$ kV and 10 kV. For the remaining configurations, downstream meandering of the fluid can be seen, formed due to the merging of the top and bottom separated flow.

The images in Figure 18 are close-ups near the cylinder, based from Figure 17. The effects of adding in the plasma actuator can be most clearly seen in two configurations at $n = 120^{\circ}$ $\phi_{max2} = 10$ kV and $n = 120^{\circ}$ $\phi_{max2} = 20$ kV. Two low velocity regions form downstream of the cylinder at $n = 120^{\circ}$ $\phi_{max2} = 10$ kV, indicating the formation of two counter rotating vortices. This vortices were already present at $n = 120^{\circ}$ $\phi_{max2} = 0$ kV and seem to have grown in size due to the direction difference when the fluid is injected at $\phi_{max2} = 0$ kV and $\phi_{max2} = 10$ kV. At the plasma configuration of $n = 120^{\circ}$ $\phi_{max2} = 20$ kV, significant mixing of the injected fluid and the main flow can be observed.

The configurations that were able to suppress VKS formation resulted in flow reattachment on the cylinder. The induced jets from the plasma actuator act as a tangential extension to the cylindrical surface, as in the 'plasma fairing' concept described by (Kozlov and Thomas, 2011), thus inhibiting separation. However for all *n* configurations when $\phi_{max2}$ is 20 kV, the jet stream induced is in the normal direction relative to the cylinder surface, resulting in flow separation occurring in the downstream regions of the cylinder.

## 6. Conclusion

The present study attempts to utilize L-PSJAs as flow control devices in a cylindrical cross flow. The L-PSJA produces a jet which is able to be vectored in accordance to the magnitude of the voltage of the exposed electrodes. The simulations are conducted at a Reynolds number of 100 to capture stable von Kármán vortex streets (VKS) forming at the trailing portions of the cylinder. The cylinder was offset 0.01 m upwards to create the instability seen downstream. A modified form of the S-H model was used to model the L-PSJAs, which are placed at different angles relative to surface of the cylinder (*n*) and are activated at different voltage settings for the downstream exposed electrode ($\phi_{max2}$).

The results showed that in the twelve configurations that were investigated (three for $\phi_{max2}$ and four for *n*), five configurations were able to suppress the formation of the VKS. This is characterized by uniform velocity downstream of the cylinder. The configurations were: $n = 40^{\circ}$ $\phi_{max2} = 10$ kV; $n = 80^{\circ}$ $\phi_{max2} = 0$ kV and 10 kV; $n = 120^{\circ}$ $\phi_{max2} = 0$ kV and 10 kV. Lift coefficient time history plots for these configurations showed a dip during the first half-second, followed by a plateau, while for the remainder of the simulations exhibit oscillations in the time histories of the lift coefficient. The drag coefficient increased for all cases with successful VKS suppression. In addition, the formation of minor fluctuations in the drag coefficient coincided with the oscillations in the lift coefficients.

For the first time, the L-PSJA has been shown (through numerical simulations) to be able to suppress VKS, and the crucial property of the L-PSJA is its ability to vectoring the jet. Possible extensions of the current work include investigating the spanwise effects by analysing a 3-D model of the L-PSJA. Other factors such as fluid-structure interactions which result in vortex-induced cylindrical vibrations could also be studied in the future.

| ase | (º) | *max2* (kV) | Vo lumetric force (%) | Aero dynamic force (%) | ase | | *max2* | Vo lumetric force (%) | Aero dynamic force (%) |
|---|---|---|---|---|---|---|---|---|---|
| | º | | 17 (left) | 83 | | 0º | | 73 | 27 |
| | º | 0 | 50 (left) | 50 | | 0º | 0 | 59 | 41 |
| | º | 0 | 59 (left) | 41 | | 0º | 0 | 17 | 83 |
| | 0º | | 61 | 39 | 0 | 20º | | 71 | 29 |
| | 0º | 0 | 25 | 75 | 1 | 20º | 0 | 64 | 36 |
| | 0º | 0 | 48 | 52 | 2 | 20º | 0 | 53 | 47 |

Table 1 Volumetric force contributions at the different cases.

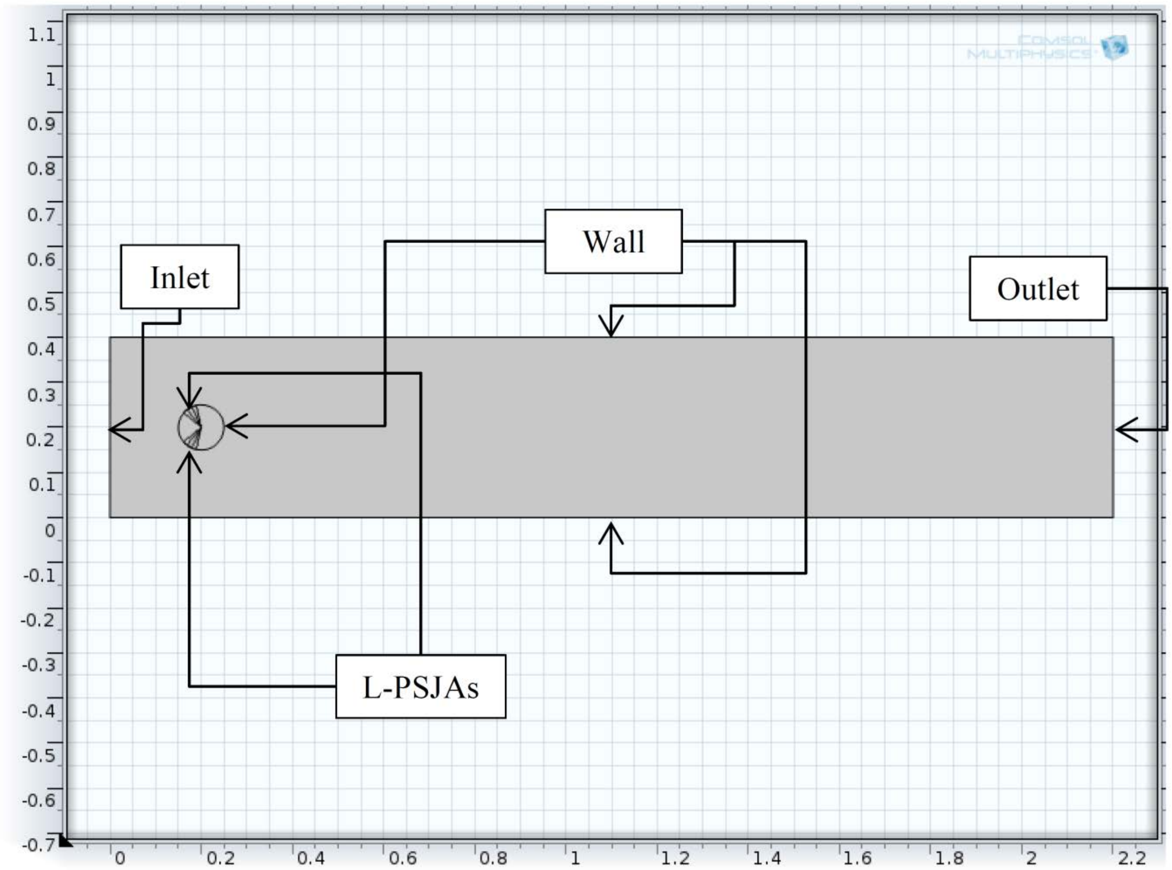


Figure 1 Modelling domain of the cylindrical wake flow. The lines inside the circular cylinder represent the placement of the L-PSJA alone the cylinder circumference.

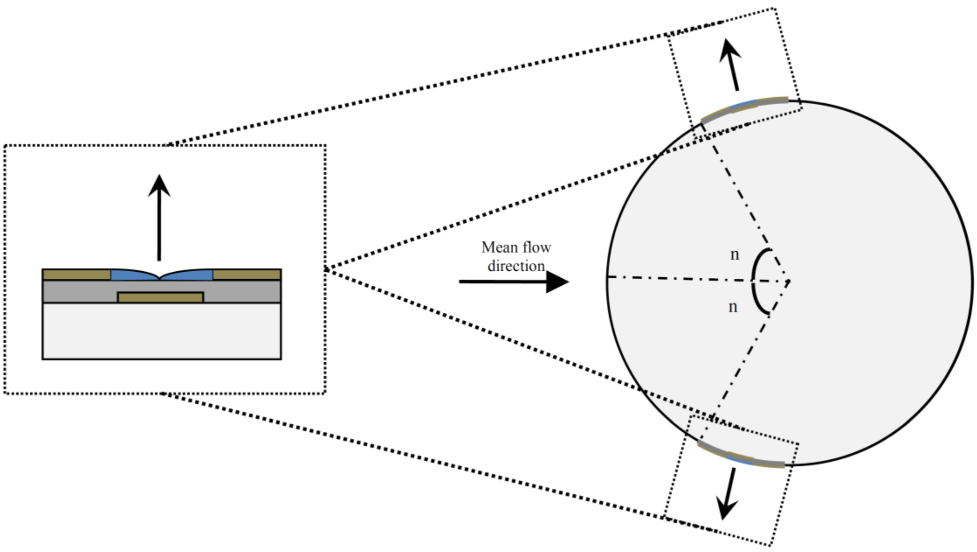


Figure 2 Implementation of the L-PSJA in cylindrical wake flow studies. The window to the left shows a zoomed-in image of the L-PSJA.

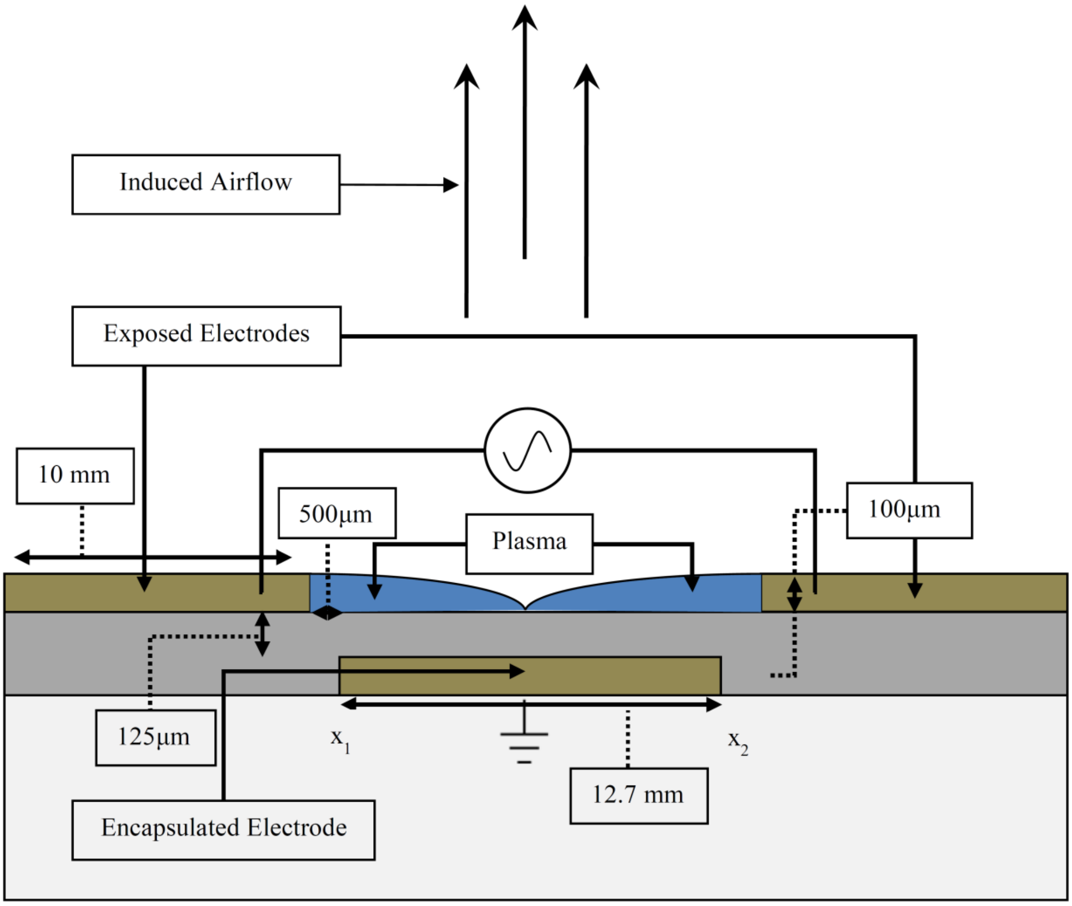

Figure 3 The features of the L-PSJA.

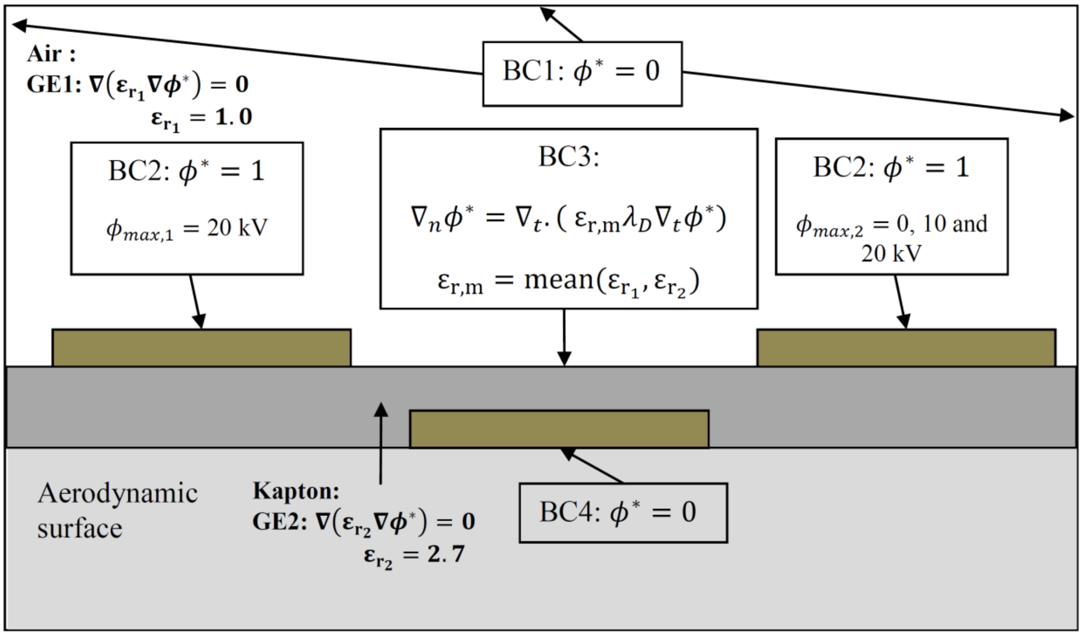


Figure 4 Governing equations for the $\phi^*$ equation in the modified S-H model of combination 1. The illustration is not drawn in scale with simulation. Note that $\phi_{max,1}$ is maintained constant at 20 kV, while $\phi_{max,2}$ is varied at 0 kV, 10 kV and 20 kV as specified in equation (5).

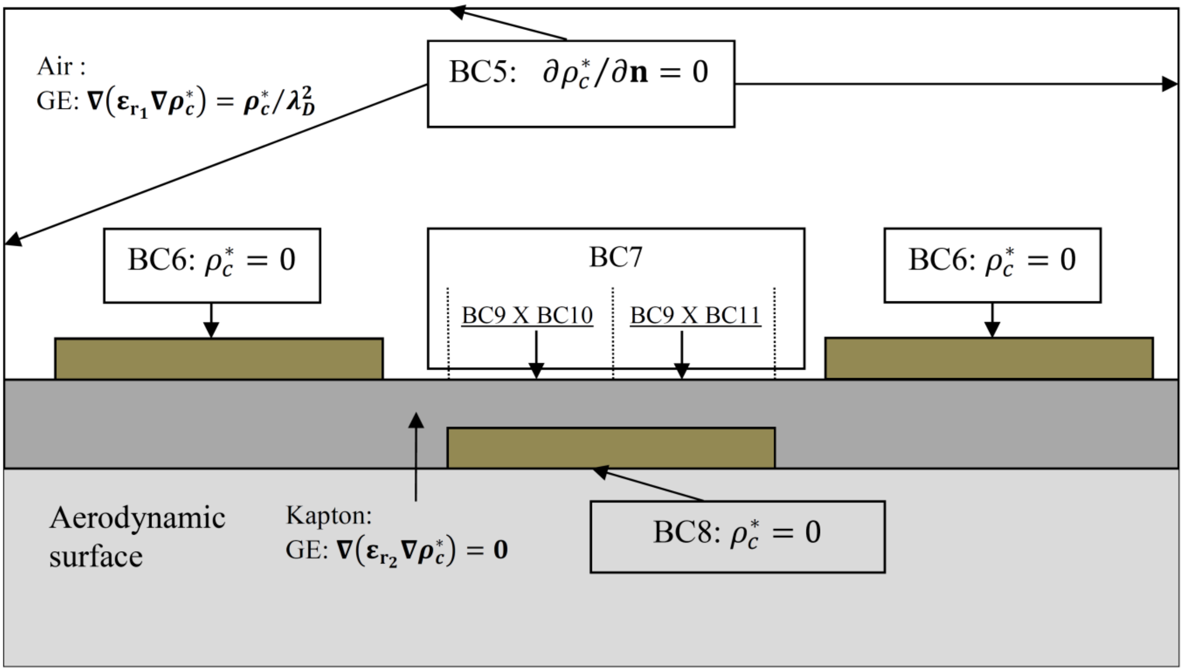


Figure 5 Governing equations for the $\boldsymbol{\rho}_c^*$ equation in the modified S-H model.

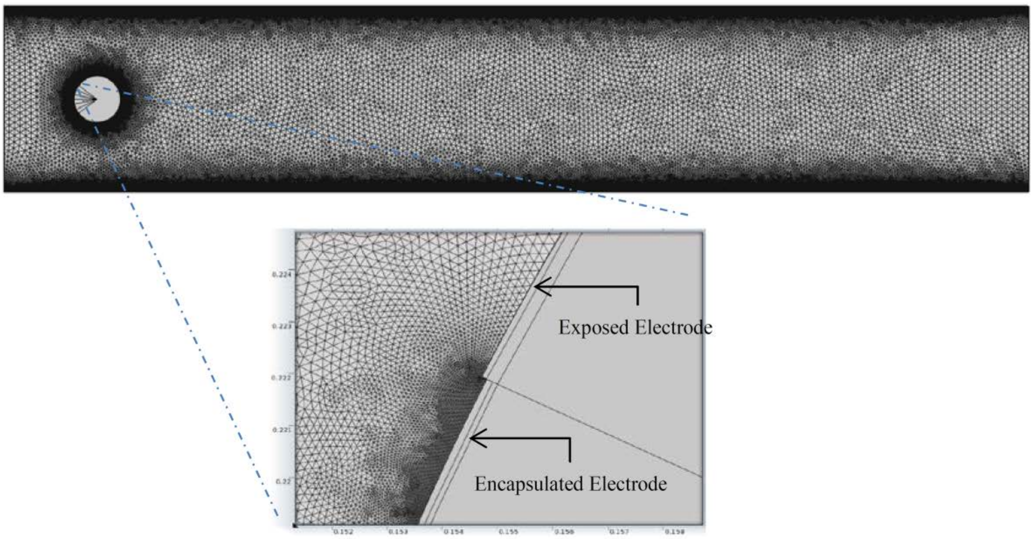


Figure 6 Coarse mesh settings, with a close up on the upper L-PSJA.

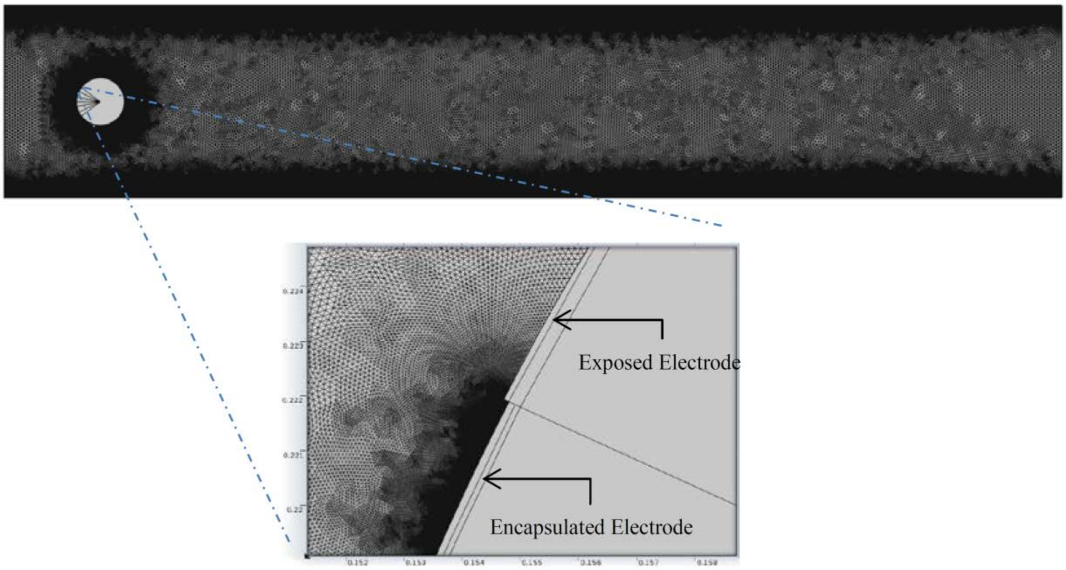


Figure 7 Fine mesh settings, with a close up on the upper L-PSJA.

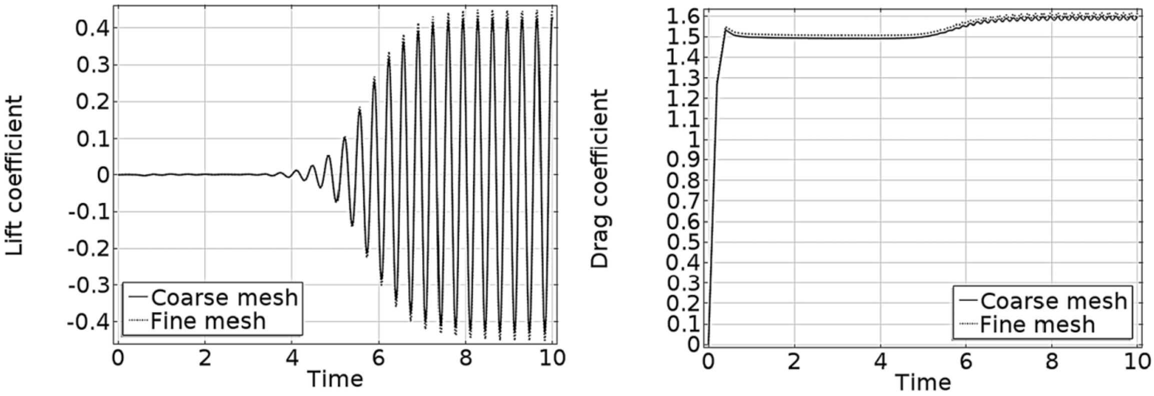


Figure 8 Lift (left) and drag (right) coefficients for the grid independent analysis.

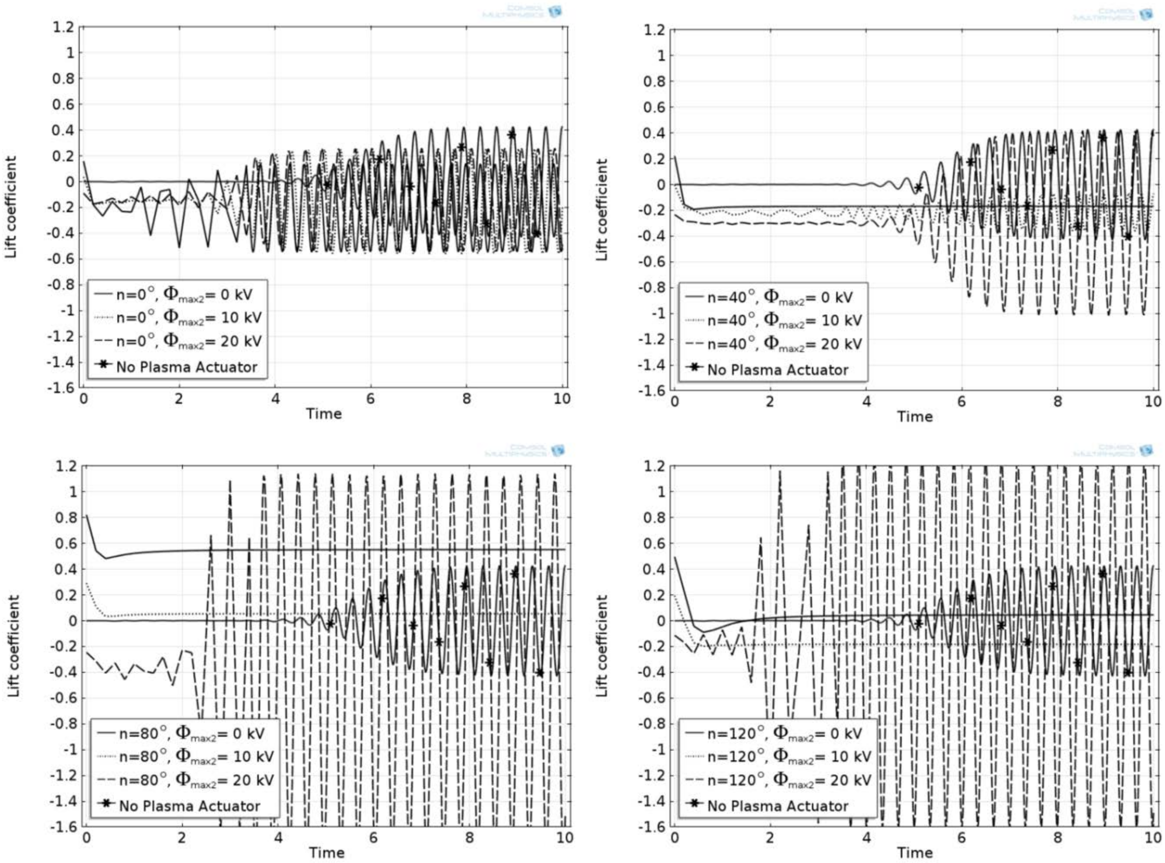


Figure 9 Lift coefficients for the different configurations.

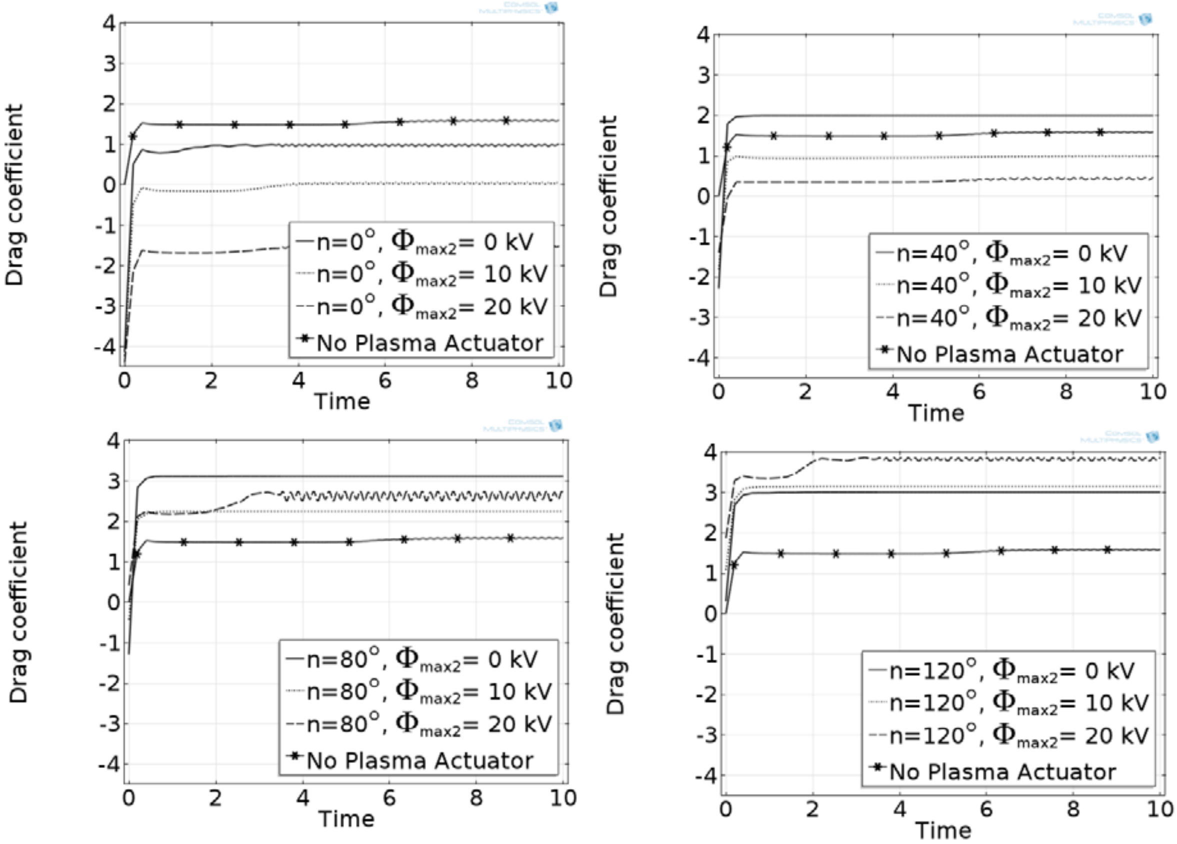


Figure 10 RMS and mean values of lift in the asymptotic region.

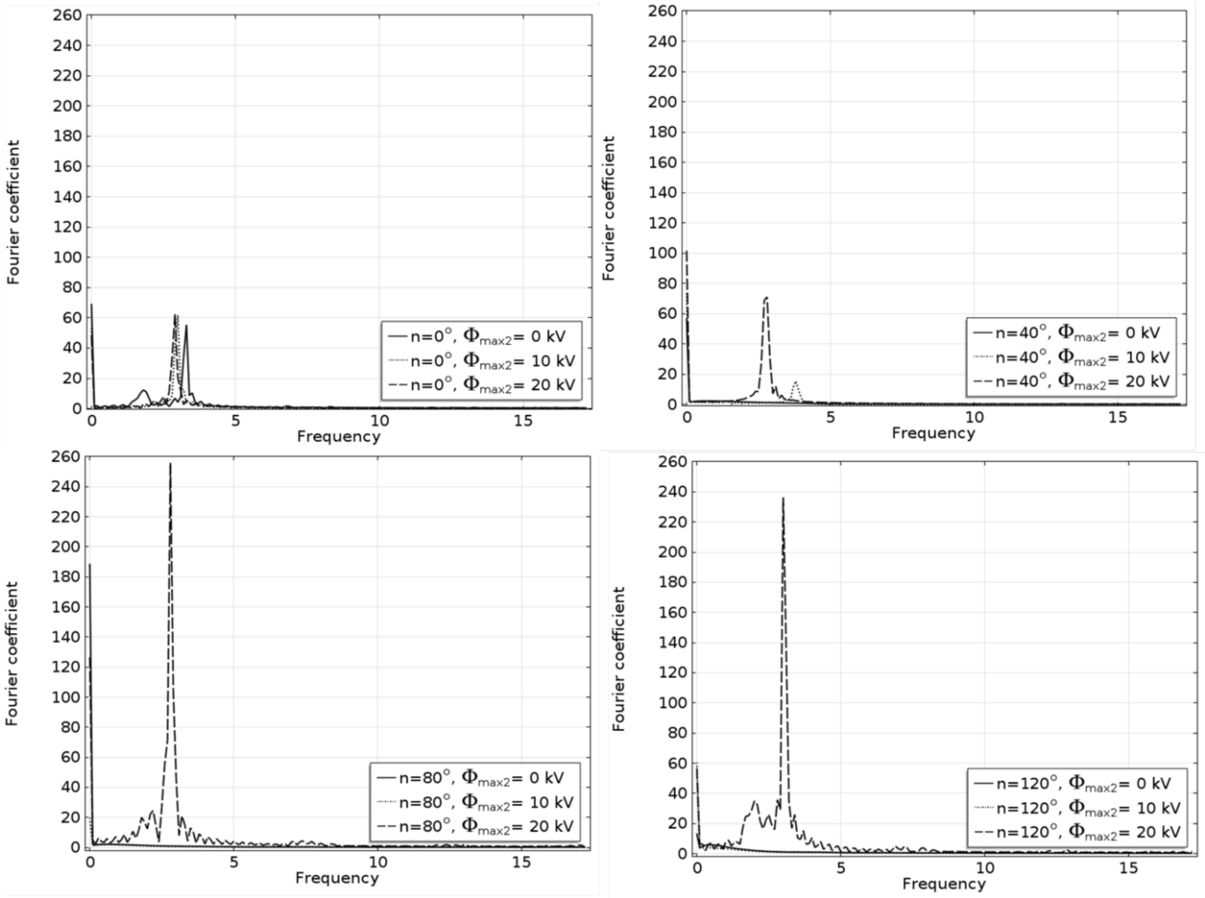


Figure 11 Dominant frequencies of the different configurations based from the lift coefficient.

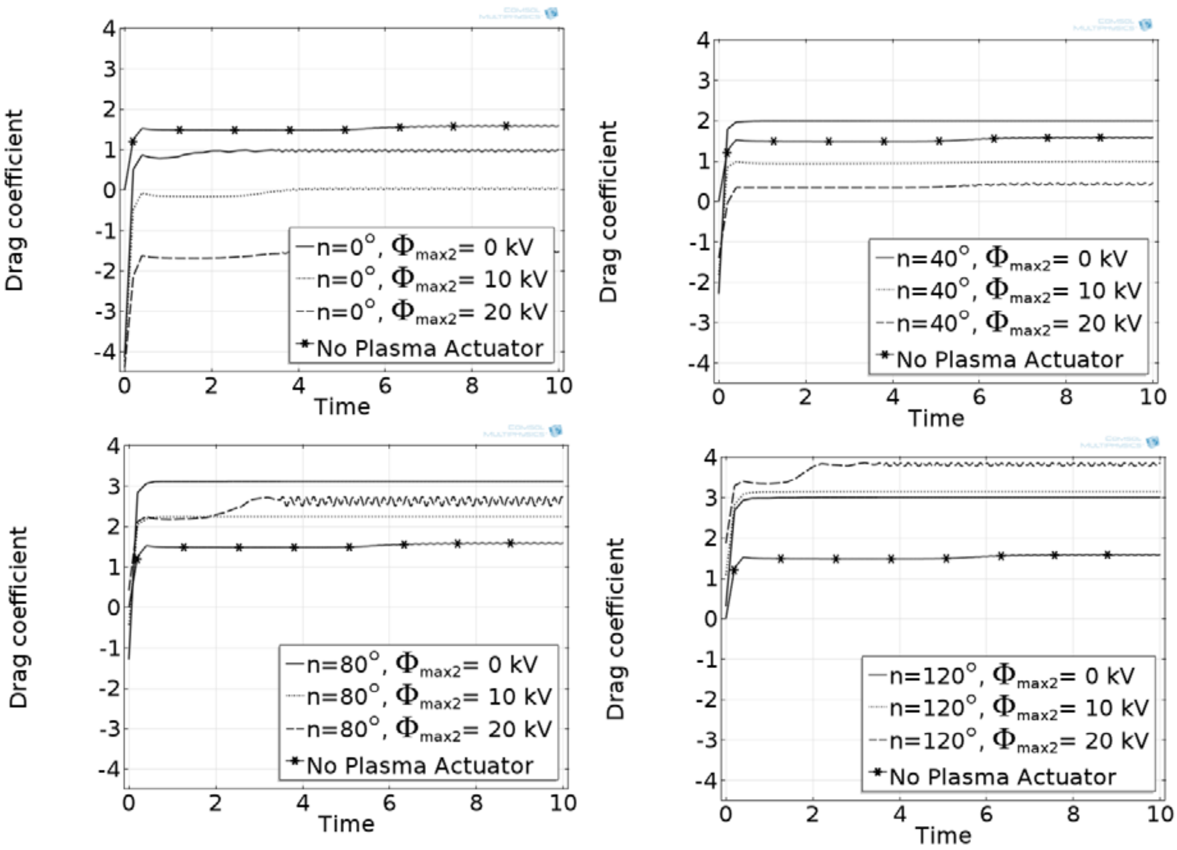


Figure 12 Drag coefficients for the different configurations.

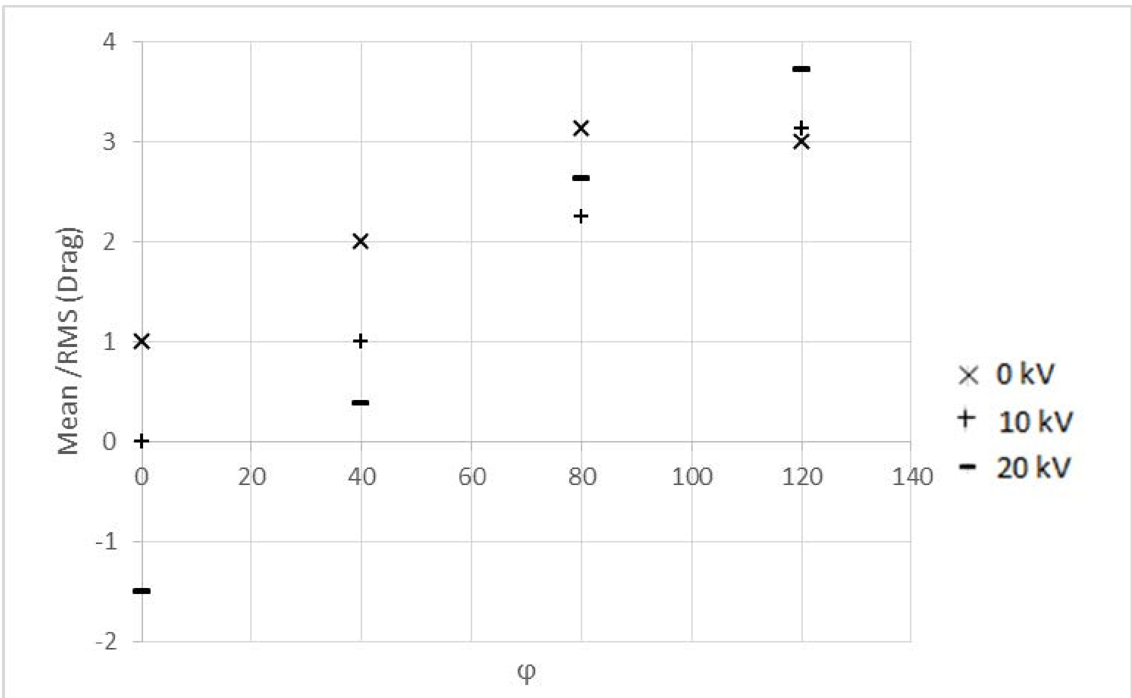


Figure 13 RMS and mean values of drag in the asymptotic region.

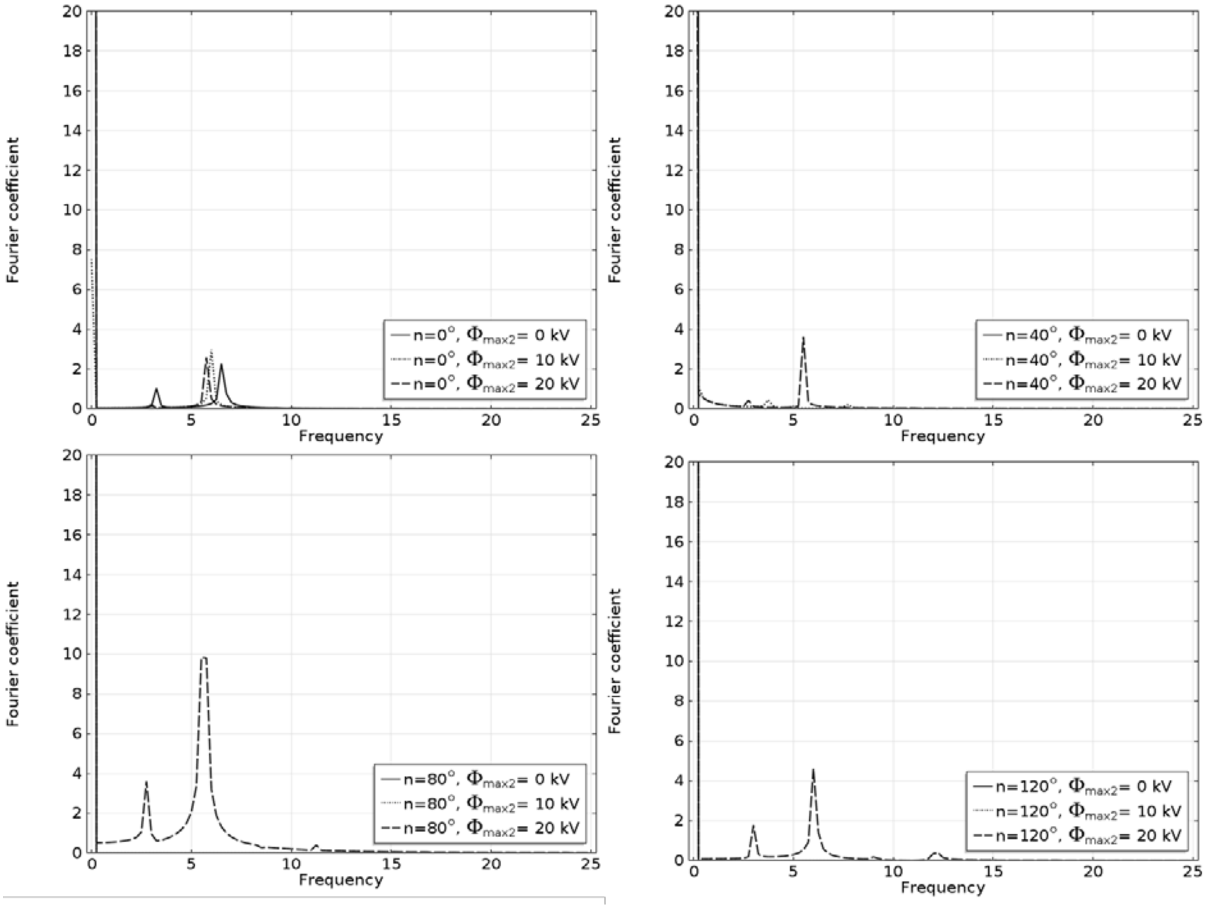


Figure 14 Dominant frequencies of the different configurations based from the drag coefficient.

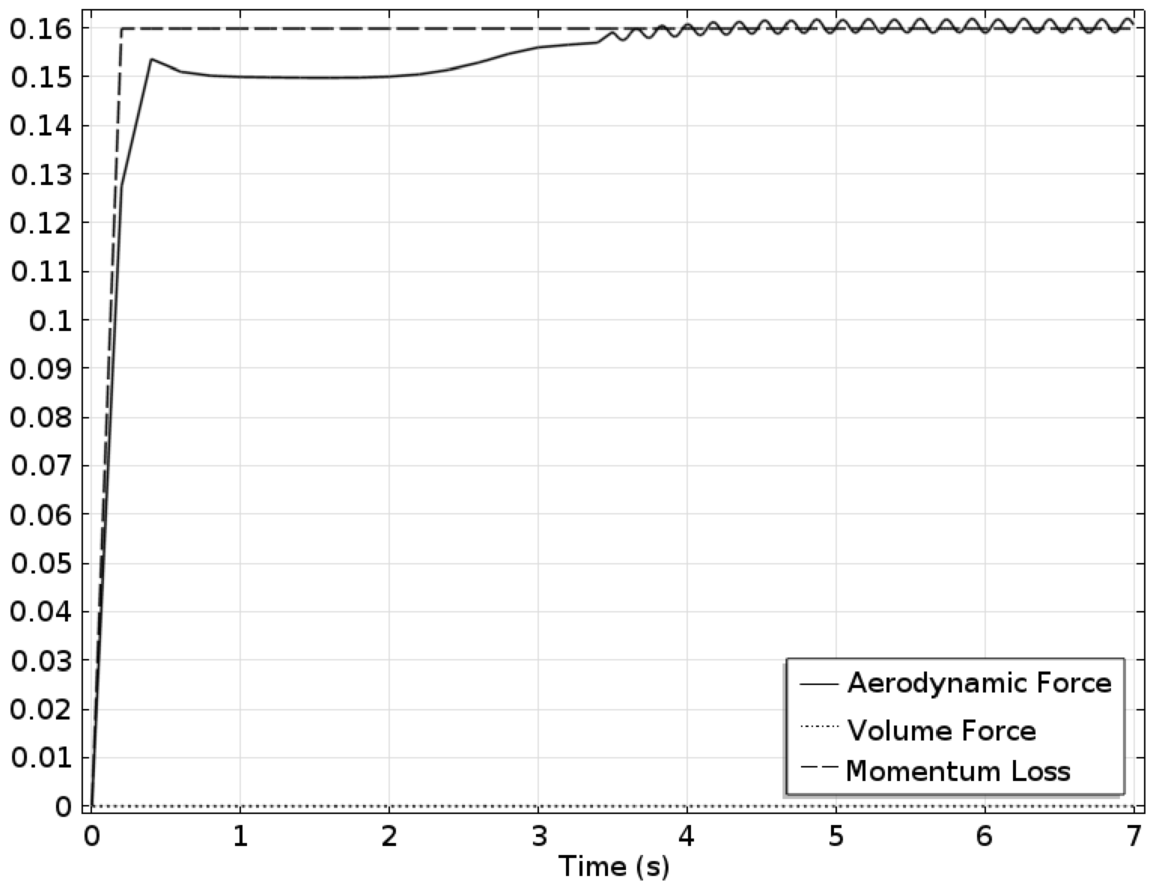


Figure 15 Force balance for the uncontrolled case (No actuator).

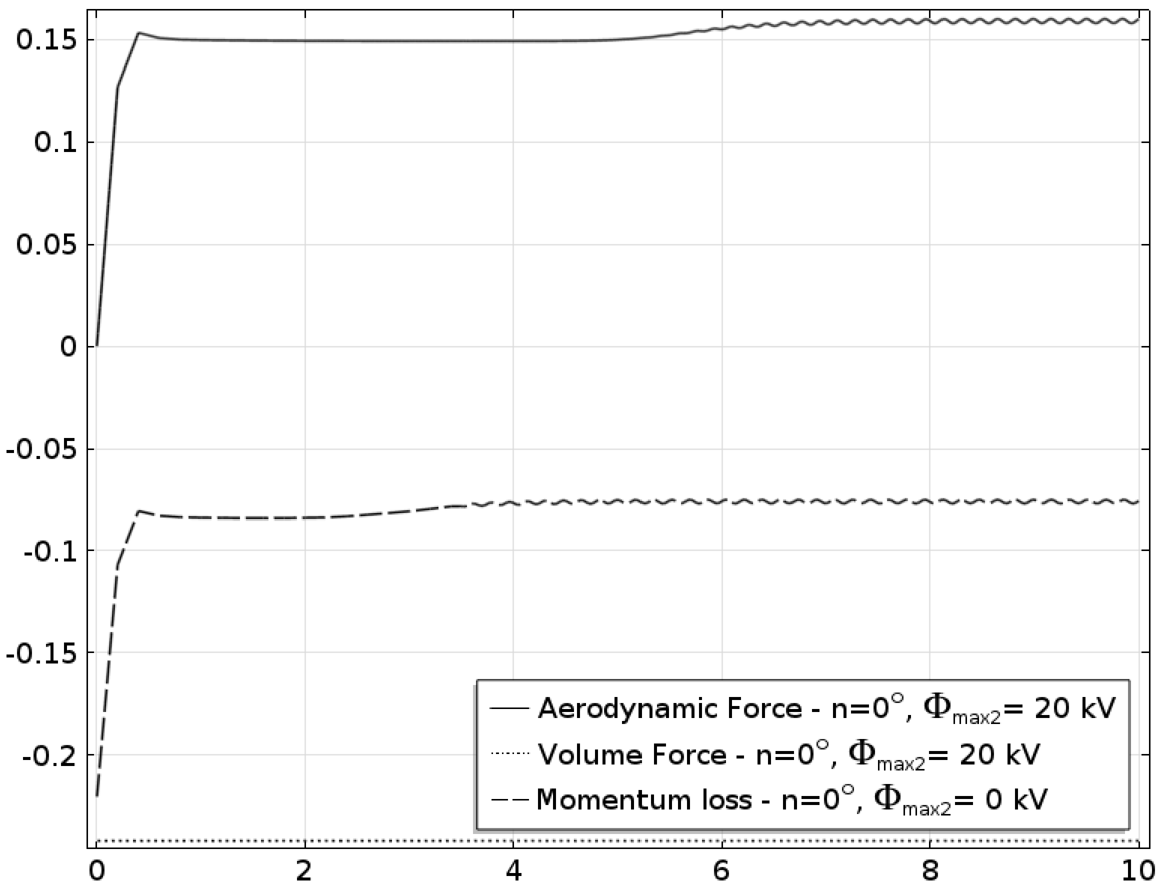


Figure 16 Force balance for the controlled case with n=0 and $\phi_{max2}$ = 20 kV (Case 3 in Table 1).

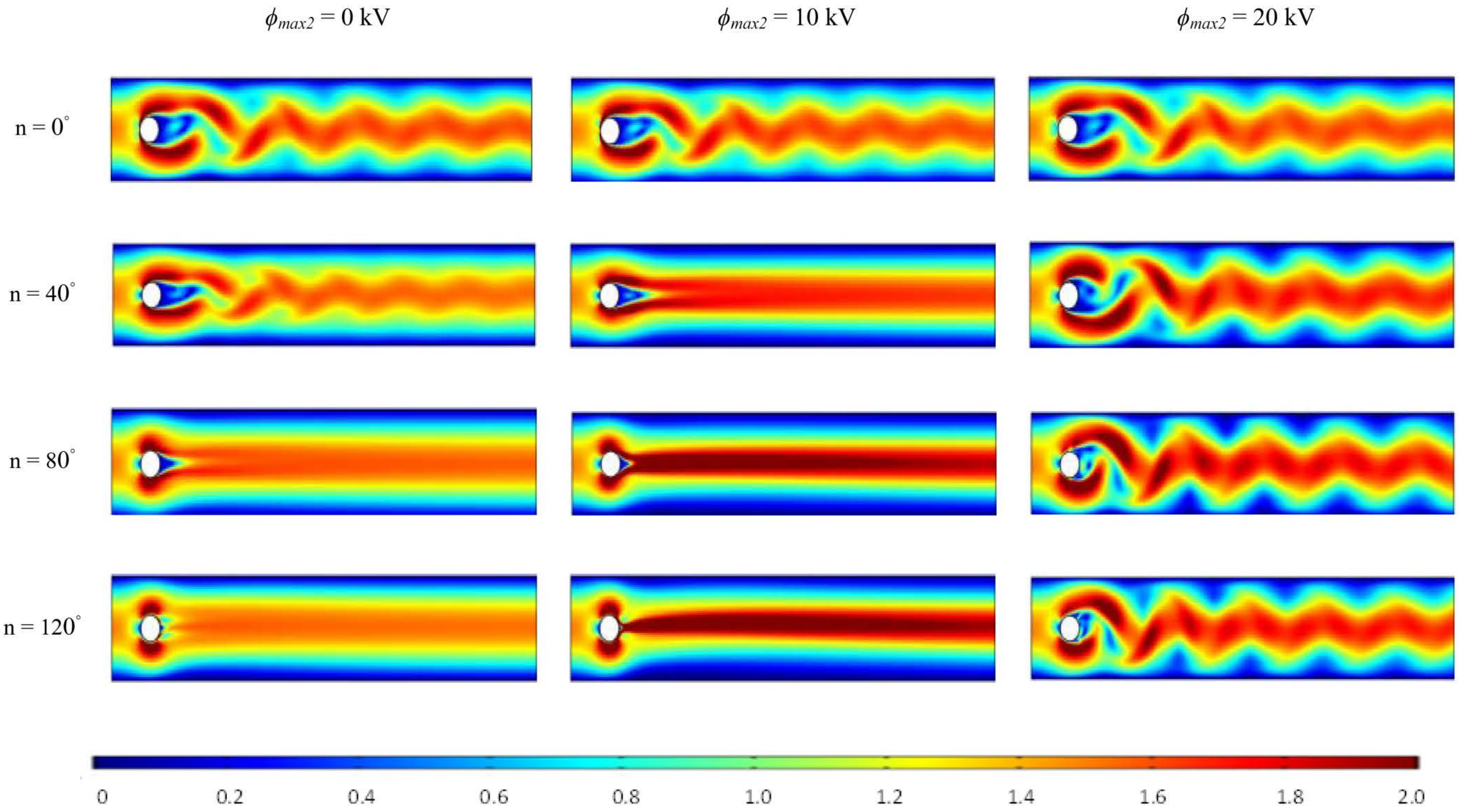


Figure 17 Velocity profiles for the different L-PSJA configurations at t = 10s.

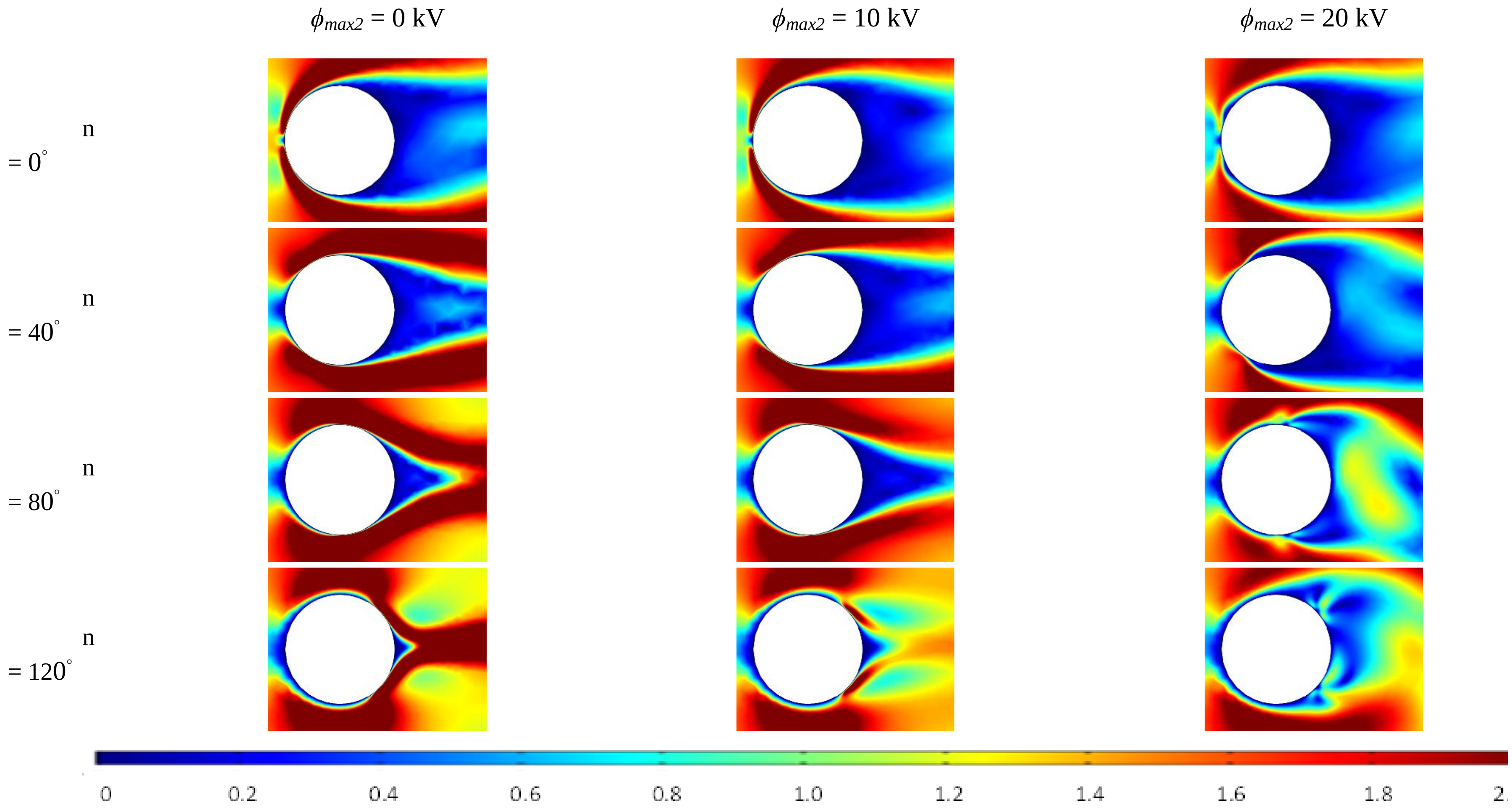


Figure 18 Close up of the flow fields for the different L-PSJA configurations at t = 10s.

References


Artana, G., Sosa, R., Moreau, E. & Touchard, G. (2003). Control of the near-wake flow around a circular cylinder with electrohydrodynamic actuators. *Experiments in Fluids,* Vol. 35**,** pp. 580-588.

Asghar, A. & Jumper, E. J. (2009). Phase Synchronization of Vortex Shedding from Two Circular Cylinders Using Plasma Actuators. *AIAA Journal,* Vol. 47**,** pp. 1608-1616.

Benard, N., Jolibois, J. & Moreau, E. (2009). Lift and drag performances of an axisymmetric airfoil controlled by plasma actuator. *Journal of Electrostatics,* Vol. 67**,** pp. 133-139.

Boeuf, J. P. & Pitchford, L. C. (2005). Electrohydrodynamic force and aerodynamic flow acceleration in surface dielectric barrier discharge. *Journal of Applied Physics,* Vol. 97**,** pp. 1-10.

Comsol 2012. COMSOL Multiphysics Modeling Guide. *COMSOL 4.2a.* Stockholm: COMSOL AB.

Corke, T. C., Enloe, C. L. & Wilkinson, S. P. (2010). Dielectric barrier discharge plasma actuators for flow control *Annual Review of Fluid Mechanics,* Vol. 42**,** pp. 505-529.

Forte, M., Jolibois, J., Moreau, E., Touchard, G. & Cazalens, M. (2007). Optimization of a dielectric barrier discharge actuator by stationary and non-stationary measurements of the induced flow velocity: application to airflow control. *Experiments in Fluids,* Vol. 43**,** pp. 917-928.

Hindmarsh, A. C., Brown, P. N., Grant, K. E., Lee, S. L., Serban, R., Shumaker, D. E. & Woodward, C. S. (2005). SUNDIALS: Suite of nonlinear and differential/algebraic equation solvers. *ACM Transactions on Mathematical Software,* Vol. 31**,** pp. 363-396.

Huang, J., Corke, T. C. & Thomas, F. O. (2006). Unsteady plasma actuators for separation control of low-pressure turbine blades. *AIAA Journal,* Vol. 44**,** pp. 1477-1487.

Huang, L., Huang, G., Lebeau, R. & Hauser, T. (2007). Optimization of airfoil flow control using a genetic algorithm with diversity control. *Journal of Aircraft,* Vol. 44**,** pp. 1337-1349.

Ibrahim, I. H. & Skote, M. (2010). Modeling the Plasma Actuator via the Splitting of the Electric Potential. *In:* JIANG, Y. & CHEN, X. (eds.) *Proceedings of the Third International Conference on Modelling and Simulation.* Wuxi, China: World Academic Union.

Ibrahim, I. H. & Skote, M. (2011). Boundary condition modifications of the Suzen-Huang plasma actuator model. *International Journal of Flow Control,* Vol. 3**,** pp. 111-131.

Ibrahim, I. H. & Skote, M. (2012). Simulations of the linear plasma synthetic jet actuator utilizing a modified Suzen-Huang model. *Physics of Fluids,* Vol. 24, (113602).

Ibrahim, I. H. & Skote, M. (2013). Effects of the scalar parameters in the Suzen-Huang model on plasma actuator characteristics. *International Journal of Numerical Methods for Heat and Fluid Flow,* Vol. 23**,** pp. 1076—1103.

Ibrahim, I. H. & Skote, M. (2014). Simulating plasma actuators in a channel flow configuration by utilizing the modified Suzen–Huang model. *Computers & Fluids,* Vol. 99**,** pp. 144-155.

Igarashi, T., Naito, H. & Fukagata, K. (2014 ). Direct Numerical Simulation of Flow around a Circular Cylinder Controlled Using Plasma Actuators. *Mathematical Problems in Engineering,* Vol. 2014**,** pp. 13.

Jayaraman, B., Thakur, S. & Shyy, W. (2006). Modeling of dielectric barrier discharge and resulting fluid dynamics. *AIAA Paper No. 2006-686.*

Jayaraman, B., Thakur, S. & Shyy, W. (2007). Modeling of fluid dynamics and heat transfer induced by dielectric barrier plasma actuator. *Journal of Heat Transfer,* Vol. 129**,** pp. 517-525.

Jukes, T. N. & Choi, K.-S. (2009). Flow control around a circular cylinder using pulsed dielectric barrier discharge surface plasma. *Physics of Fluids,* Vol. 21**,** pp.

Kozlov, A. V. 2010. *Plasma Actuators for Bluff Body Flow Control.* Graduate Program in Aerospace and Mechanical Engineering, Ph.D. thesis, University of Notre Name.

Kozlov, A. V. & Thomas, F. O. (2011). Bluff-Body Flow Control via Two Types of Dielectric Barrier Discharge Plasma Actuation. *AIAA Journal,* Vol. 49**,** pp. 1919-1931.

Mamunuru, M., Guo, S., Poon, D., Burman, D., Simon, T., Ernie, D. & Kortshagen, U. (2009). Separation control using plasma actuator: Simulation of plasma actuator. *AIAA Paper No. 2009-4186*.

Mittal, S. & Raghuvanshi, A. (2001). Control of vortex shedding behind circular cylinder for flows at low Reynolds numbers. *International Journal of Numerical Methods in Fluids,* Vol. 35**,** pp. 421-447.

Moreau, E. (2007). Airflow control by non-thermal plasma actuators. *Journal of Physics D: Applied Physics,* Vol. 40**,** pp. 605-636.

Orlov, D. M., Apker, T., He, C., Othman, H. & Corke, T. C. (2007). Modeling and Experiment of Leading Edge Separation Using SDBD Plasma Actuators. *AIAA Paper No. 2007-0877*.

Orlov, D. M., Corke, T. C. & Patel, M. P. (2006). Electric Circuit Model for the Aerodynamic Plasma Actuator. *AIAA Paper No. 2006-1206*.

Porter, C., Abbas, A., Cohen, K., Mclaughlin, T. & Enloe, C. L. (2009). Spatially distributed forcing and jet vectoring with a plasma actuator. *AIAA Journal,* Vol. 47**,** pp. 1368-1378.

Porter, C. O., Mclaughlin, T. E., Enloe, C. L. & Font, G. I. (2007). Boundary Layer Control Using a DBD Plasma Actuator. *AIAA Paper No. 2007-0786*.

Post, M. L. & Corke, T. C. (2006). Separation control using plasma actuators: Dynamic stall vortex control on oscillating airfoil. *AIAA Journal*, Vol. 44**,** pp. 3125-3135.

Reasor Jr, D. A., Lebeau Jr, R. P. & Suzen, Y. B. (2007). Unstructured grid simulations of plasma actuator models. *AIAA Paper No. 2007-3973*.

Rizzetta, D. P. & Visbal, M. R. (2007). Numerical investigation of plasma-based flow control for transitional highly loaded low-pressure turbine. *AIAA Journal,* Vol. 45**,** pp. 2554-2564.

Santhanakrishnan, A., Reasor Jr, D. A. & Lebeau Jr, R. P. (2009). Characterization of linear plasma synthetic jet actuators in an initially quiescent medium. *Physics of Fluids,* Vol. 21**,** (043602).

Schafer, M. & Turek, S. (1996). Benchmark Computations of Laminar Flow Around a Cylinder. *In:* HIRSCHEL, E. H. (ed.) *Notes on Numerical Fluid Mechanis, Vol. 52.* Wiesbaden: Vieweg.

Skote, M. (2014). Scaling of the velocity profile in strongly drag reduced turbulent flows over an oscillating wall. *International Journal of Heat and Fluid Flow,* Vol. 50, pp. 352—358.

Suzen, Y. B. & Huang, P. G. (2006). Simulations of flow separation control using plasma actuators. *AIAA Paper No. 2006-877*.

Suzen, Y. B., Huang, P. G. & Ashpis, D. E. (2007). Numerical simulations of flow separation control in low-pressure turbines using plasma actuators. *AIAA Paper No. 2006-937*.

Suzen, Y. B., Huang, P. G., Jacob, J. D. & Ashpis, D. E. (2005). Numerical simulations of plasma based flow control applications. *AIAA Paper No. 2005-4633*.

Thomas, F. O., Kozlov, A. & Corke, T. C. (2008). Plasma actuators for cylinder flow control and noise reduction. *AIAA Journal,* Vol. 46**,** pp. 1921-1931.

Williamson, C. H. K. (1996). Vortex Dynamics in the Cylinder Wake. *Annual Review of Fluid Mechanics,* Vol. 28**,** pp. 477-539.

Zdravkovich, M. M. (1997). *Flow around circular cylinders,* Oxford, Oxford Science Publications.

Zhang, P. F., Wang, J. J., Feng, L. H. & Wang, G. B. (2010). Experimental study of plasma flow control on highly swept delta wing. *AIAA Journal,* Vol. 48**,** pp. 249-252.